Boosting the Thermoelectric Performance of α-MgAgSb through Phase-Transition-Induced Self-Doping

Kaiwei Guo,[1,2,*] Tianyu Wang,[3,*] Zhen Fan,[1] Lunhua He,[1,5] Fuhong Chen,[1,4] Yi Wang,[1,2] Qi Zhao,[1] Jiawei Yang,[1] Hangtian Zhu,[1] Jun Li,[1,†] Te-Huan Liu,[3,‡] and Huaizhou Zhao[1,§]

[1]*Beijing National Laboratory for Condensed Matter Physics, Institute of Physics, Chinese Academy of Sciences, Beijing 100190, China*
[2]*School of Physics Science, University of Chinese Academy of Sciences, Beijing 100049, China*
[3]*School of Energy and Power Engineering, Huazhong University of Science and Technology, Wuhan, Hubei 430074, China*
[4]*School of Physics, Beijing Institute of Technology, Beijing 100190, China*
[5]*Dongguan Neutron Science Center, Dongguan 523808, China*

(Received 12 December 2025; revised 10 March 2026; accepted 20 March 2026; published 10 April 2026)

In thermoelectric (TE) and other functional electronic materials, chemical doping is commonly employed to tune the carrier density toward an optimal Fermi level and, in turn, maximize the electrical transport. However, in some systems, such as the emerging high-performance p-type TE material α-MgAgSb, chemical doping is challenging due to its weak chemical bonds and extremely low solubility of heteroatomic dopants, which makes it difficult to increase the hole carrier density and realize the otherwise predictable improvements in the TE power factor. Here, we report a doping-free strategy to enhance the TE performance of α-MgAgSb by utilizing a phase-transition-induced self-doping process. Annealing at the phase-transition temperature of 593 K lowers the formation energy of Ag vacancies in the high-temperature β phase, and these vacancies are subsequently retained upon cooling back to the α phase. As a result, the hole concentration increases markedly from 4.5×10^{19} to 1.3×10^{20} cm^{-3}, activating multiple valence bands and boosting the room-temperature power factor by ~35% to 30 $\mu\mathrm{W\,cm}^{-1}\,\mathrm{K}^{-2}$. A single-leg device fabricated from the optimized material achieves a high conversion efficiency of 10.7% and a maximum output power of 71.1 mW at $\Delta T = 285$ K. This work demonstrates a viable pathway for enhancing TE performance via phase-transition engineering.

DOI: 10.1103/gqjx-6kqr

Subject Areas: Condensed Matter Physics, Materials Science

Thermoelectric (TE) materials, capable of direct conversion between heat and electricity via the Seebeck and Peltier effects, offer a promising route to sustainable energy harvesting [1,2]. The efficiency of TE materials is gauged by the dimensionless figure of merit, $zT = S^2\sigma T/\kappa$, where S, σ, and κ represent the Seebeck coefficient, electrical conductivity, and thermal conductivity, respectively, and T is the absolute temperature [3,4]. The conversion efficiency (η) and output power (P_{out}) of TE modules are critically governed by the material's zT and power factor ($S^2\sigma$), respectively [5–8]. Thus, simultaneous improvement in both performance parameters is essential for broadening the practical applicability of TE technology.

To date, bismuth telluride (Bi_2Te_3) remains the commercial benchmark near room temperature and, as the dominant commercial TE material, exhibits a high zT of 1.0 at 300 K and a conversion efficiency of 6% at a temperature difference (ΔT) of 200 K [9–11]. In contrast, magnesium-based compounds such as p-type MgAgSb and n-type $Mg_3(Sb,Bi)_2$ have recently emerged as compelling alternatives due to their nontoxic constituents and excellent TE performance over a broad temperature range [12,13]. Notably, all-Mg-based modules have achieved a conversion efficiency exceeding 12% under a temperature difference of 300 K [5]. Although significant efforts have been devoted to p-type MgAgSb in recent years, most studies have focused on the device-level engineering, particularly on electrode selection [14–16]. Specifically, in Li's work, [6] α/β-MgAgSb junction was constructed in the device, and the α/β phase transition was taken advantage of to reduce the internal resistance of the device. However, the

*These authors contributed equally to this work.
†Contact author: junli@iphy.ac.cn
‡Contact author: thliu@hust.edu.cn
§Contact author: hzhao@iphy.ac.cn

underlying physical mechanism remains poorly understood. At the material level, conventional chemical doping remains the primary strategy for optimizing the carrier concentration [17–20]. Heat treatment is a commonly employed strategy to manipulate Ag vacancies, including tuning the SPS temperature to vary the Ag-vacancy concentration and thereby achieve the optimal carrier concentration. However, most of these studies are limited to scenarios with low band degeneracy, resulting in relatively low power factors [21]. However, the full potential of *p*-type MgAgSb has been hindered by its relatively low power factor ($\sim 23\ \mu W \cdot cm^{-1} \cdot K^{-2}$), which limits the output power in generation mode. This limitation persists despite a complex valence band structure with a theoretical valley degeneracy as high as 14 [22], suggesting significant untapped potential for enhancing the power factor via optimized carrier concentration tuning.

Conventional approaches to carrier optimization in MgAgSb rely on chemical doping, which is often constrained by low dopant solubility and undesirable Ag-ion migration [23–25]. The underlying mechanism is tied to the unique crystal structure of MgAgSb, which crystallizes in α phase ($I\bar{4}c2$) structures below 583 K. It is noted that the Ag atom is located at the center of the Sb tetrahedron and the Mg atom is in the distorted Sb octahedron [24,26]. The weak Ag-Sb bonds and high Ag mobility favor the formation of Ag vacancies and Ag-Mg antisite defects [24]. Owing to its limited solid solubility and unique crystal structure, achieving a high carrier concentration in α-MgAgSb via conventional doping often comes at the expense of phase purity. In this work, we break from this paradigm by introducing a doping-free strategy that exploits the reversible $\alpha - \beta$ phase transition around 593 K to intrinsically engineer Ag vacancies. We demonstrate that annealing in the β phase significantly reduces the formation energy of Ag vacancies, enabling the creation and subsequent "freezing-in" of a high concentration of these defects upon rapid cooling back to the α phase as shown in Fig. 1(a). Combined with density-functional theory calculations, Ag vacancies consistently exhibit the lowest formation energy across the relevant Fermi-level range in both α and β phases, while Mg/Sb vacancies and antisite defects are higher in formation energy, even after accounting for charge-state stability (Fig. S1) [27]. Therefore, the excitation of Ag vacancies can be achieved through phase-transition-induced self-doping. This process elevates the hole concentration from 4.5×10^{19} to $1.3 \times 10^{20}\ cm^{-3}$ and activates multivalley transport, as evidenced by an increase in the effective valley degeeracy N_v from 8 to 14 as shown in Fig. 1(b). The enhancement of the induced intervalley electron-phonon scattering is partially compensated by the increased density of states (DOS) effective mass after annealing, which results in only a modest decrease in carrier mobility from 60 to $45\ cm^2 \cdot V^{-1} \cdot s^{-1}$. This collective enhancement yields a remarkable ~35% improvement in the room-temperature power factor, reaching $30\ \mu W \cdot cm^{-1} \cdot K^{-2}$, which is among the highest values reported for MgAgSb-based materials as shown in Fig. 1(c). Since no foreign dopants are introduced, the intrinsically low lattice thermal conductivity is preserved, leading to a room-temperature zT of ~0.83 and an average zT of 1.30 close to that of the as-synthesized sample ($zT_{avg} = 1.32$) between 300 and 573 K.

To evaluate the practical applicability of this strategy, we fabricated a single-leg TE module using the optimized material; it achieved a conversion efficiency of 10.7% and a maximum power density of $71.1\ mW \cdot cm^{-2}$ at $\Delta T = 285$ K, which surpasses the performance of the as-synthesized sample by 30% as show in Fig. 1(d). This work establishes a novel, generalizable pathway for performance enhancement in multiphase TE systems by leveraging inherent phase transitions for defect engineering, thereby moving beyond the conventional limitations of chemical doping.

To elucidate the origin of the enhanced carrier concentration and the structural evolution during thermal processing, we performed *in situ* variable-temperature powder neutron diffraction (PND) on MgAgSb. The diffraction patterns were collected in the following sequence (from bottom to top in Fig. 2): (i) the as-synthesized MgAgSb sample at room temperature, (ii) at 593 K during the phase transition, and (iii) after annealing and cooling back to room temperature. Both the as-synthesized and annealed samples [Figs. 2(i) and 2(iii)] were identified as the α-MgAgSb phase (space group I-4c2), whereas at 593 K [Fig. 2(ii)], the structure transformed to β-MgAgSb (space group $P4/nmm$), consistent with previous reports. No obvious secondary phases were detected in either the as-synthesized or annealed samples.

Rietveld refinement against the PND data confirmed the tetragonal structure and allowed quantification of the site occupancy factors (SOFs) for the Ag sites. In the as-synthesized sample, the SOF of the Ag_1 site was 0.986, corresponding to the stoichiometry of $MgAg_{0.993}Sb$, in agreement with the earlier work [28]. After annealing, the SOFs of Ag_1 and Ag_2 decreased to 0.978 and 0.980, respectively, corresponding to a stoichiometry of $MgAg_{0.984}Sb$. This indicates an increased concentration of Ag vacancies, consistent with the rise in hole concentration from $\sim 5.1 \times 10^{19}$ to $\sim 1.1 \times 10^{20}\ cm^{-3}$—more than a twofold increase following the β phase transition. During the measurements, a glass enclosure was placed over the sample stage to ensure precise temperature control. Unfortunately, although the spurious peaks from the glass do not affect the main diffraction peaks of the material, they do introduce some interference to the refinement of vacancy concentrations at high temperature, which may compromise the accuracy of the refined results. Furthermore, our work primarily focuses on optimizing and enhancing the carrier concentration in the α phase. The high carrier concentration in the β phase has limited

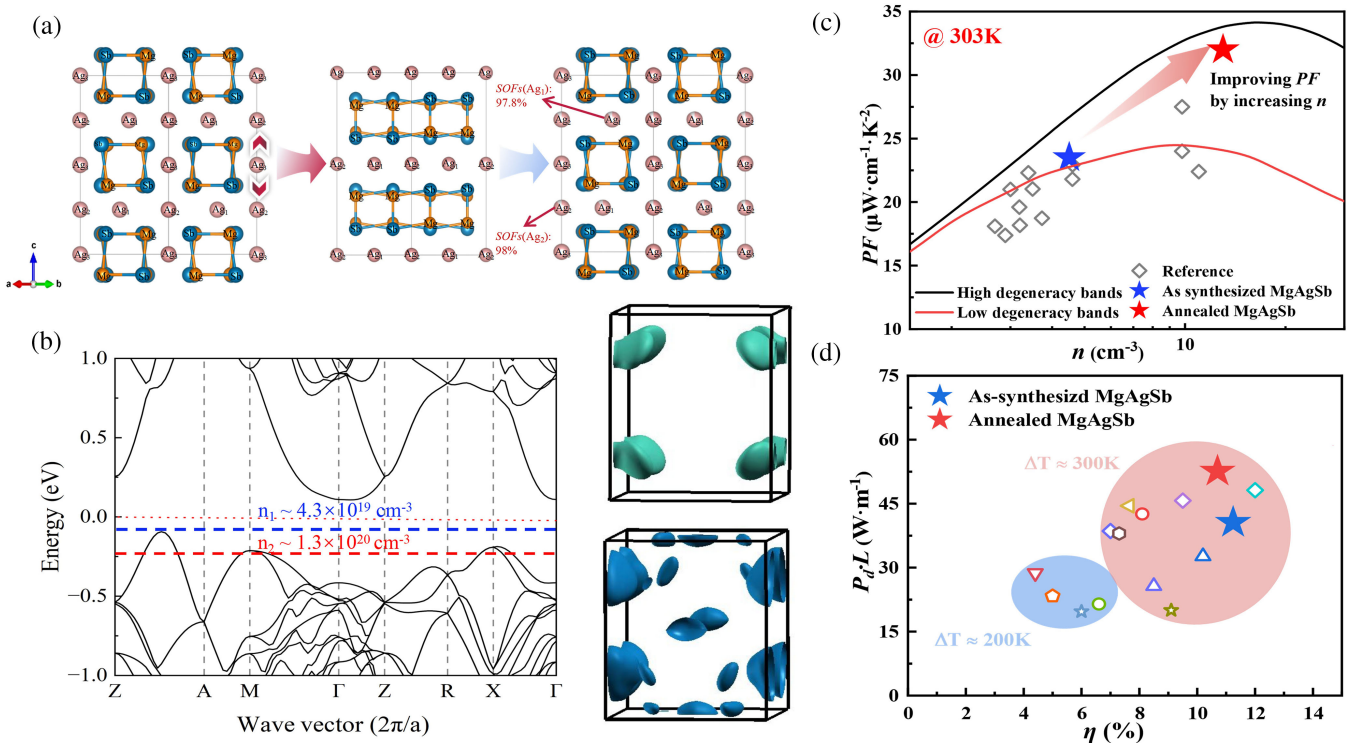

FIG. 1. (a) The crystal structure evolution of MgAgSb annealed above the phase transformation temperature of 593 K and cooled back to 300 K. (b) The calculated band structure of α-MgAgSb, and the carrier concentration from $n_1 \sim 4.3 \times 10^{19}$ cm^{-3} to $n_2 \sim 1.3 \times 10^{20}$ cm^{-3} after annealing. The pockets on the right increase from 8 to 14. (c) The correlation between calculated and experimental power factors and carrier concentration at room temperature [5,14–19,29–33]. (d) The comparisons of maximum $P_d \cdot L$ and efficiency of power generation modules at near room temperatures among modules, including BST/BST, $Mg_3(Sb, Bi)_2$/MgAgSb, single-leg MgAgSb (hollow and smaller symbols) [5,14,16,29,32,34–38].

reference value for the final results of the α-phase measurement, we did not perform a refinement analysis of the defect concentration for the β phase. Key refinement parameters are summarized in Table S2 and Table S3 of the Supplemental Material [27], and schematic illustrations of the Ag site occupancies are also provided in Fig. 1(a).

To provide a quantitative estimate of the effective hole concentration associated with vacancies, we performed first-principles calculations and evaluated the free hole concentration from the electronic density of states using Fermi-Dirac statistics. We started from a perfect α-MgAgSb supercell with 96 atoms, and then constructed three vacancy models by removing one Ag atom, one Mg atom, and one Sb atom, respectively. These defective supercells represent a nominal concentration of one vacancy per 96-atom supercell. For each model, we calculated the electronic DOS and determined the Fermi level from the DOS output. The free hole concentration at 300 K was then evaluated by integrating the valence-band DOS weighted by the probability of occupation absence:

$$p_{\text{cell}}(T) = \int_{-\infty}^{E_v} D(E)[1 - f(E; E_F, T)]dE, \qquad (1)$$

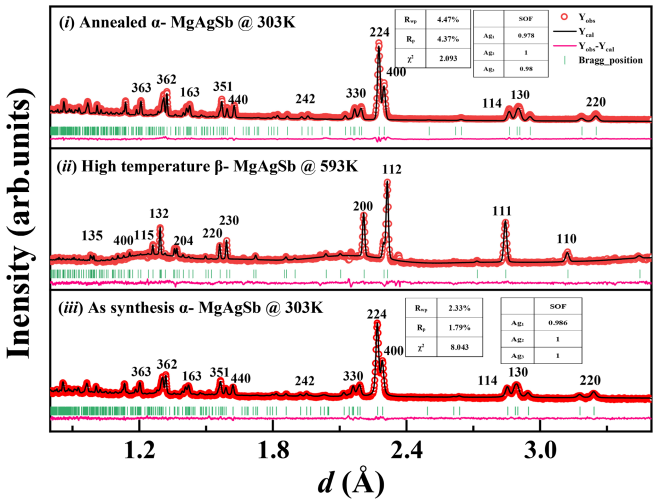

FIG. 2. The *in situ* variable-temperature powder neutron diffraction pattern of MgAgSb powder at different temperatures. From the bottom to the top, the profile plot of Rietveld refinement against the PND dataset of as-synthesized α-MgAgSb at 303 K, the MgAgSb at 593 K. the annealed and cooled back α-MgAgSb at 303 K.

$$f(E;E_F,T)=\frac{1}{1+\exp(\frac{E-E_F}{k_BT})}. \quad (2)$$

Here, $D(\mathrm{E})$ is the total DOS in units of states per eV per supercell, and E_v is the valence band maximum. The integral gives the number of holes per supercell, which was then converted into cm^{-3} using the supercell volume. Using this approach, the calculated hole concentrations are 5.00×10^{20} cm^{-3} for the Ag-vacancy model, 9.43×10^{20} cm^{-3} for the Mg vacancy model, and 7.85×10^{12} cm^{-3} for the Sb vacancy model. These results show that the carrier concentration is highly defect dependent, and that a percent-level reduction of Ag site occupancy can support a hole concentration on the order of 1.00×10^{20} cm^{-3}. Therefore, the refined Ag-vacancy fraction and the Hall carrier concentration are not expected to follow a simple linear relationship.

We further note that the Hall carrier concentration reflects mobile carriers and can differ from the total ionized acceptor concentration. The effective number of free holes contributed by each Ag-vacancy can be reduced by charge compensation from other defects or by the formation of electrically neutral defect complexes. In addition, multivalley transport and possible changes in the Hall factor can affect the carrier concentration extracted from Hall measurements when the Fermi level shifts. These effects provide explanations for why a modest change in refined Ag-site occupancy can coincide with a large relative change in the measured Hall carrier concentration. Based on our DOS-based evaluation, a hole concentration around 1.1×10^{20} cm^{-3} is within a reasonable range for the present material when compensation and transport-related factors are considered.

In situ transmission electron microscopy (TEM) was conducted on a focused ion beam (FIB)-prepared MgAgSb sample to visualize micro-structural evolution during heating. As shown in Fig. 3(a), the sample was heated from room temperature (293 K) to 603 K (above the phase transition temperature) and then cooled back to room temperature. Second-phase precipitates emerged at 403 K and stabilized by 603 K, and they persisted after cooling. Energy-dispersive x-ray spectroscopy (EDS) confirmed these precipitates to be Ag-Sb compounds, which can be assigned to Ag_3Sb [Fig. 3(b)]. The precipitation mechanism is attributed to the low formation energy and high mobility of Ag vacancies at elevated temperatures. Ag atoms readily vacate their lattice sites, creating Ag

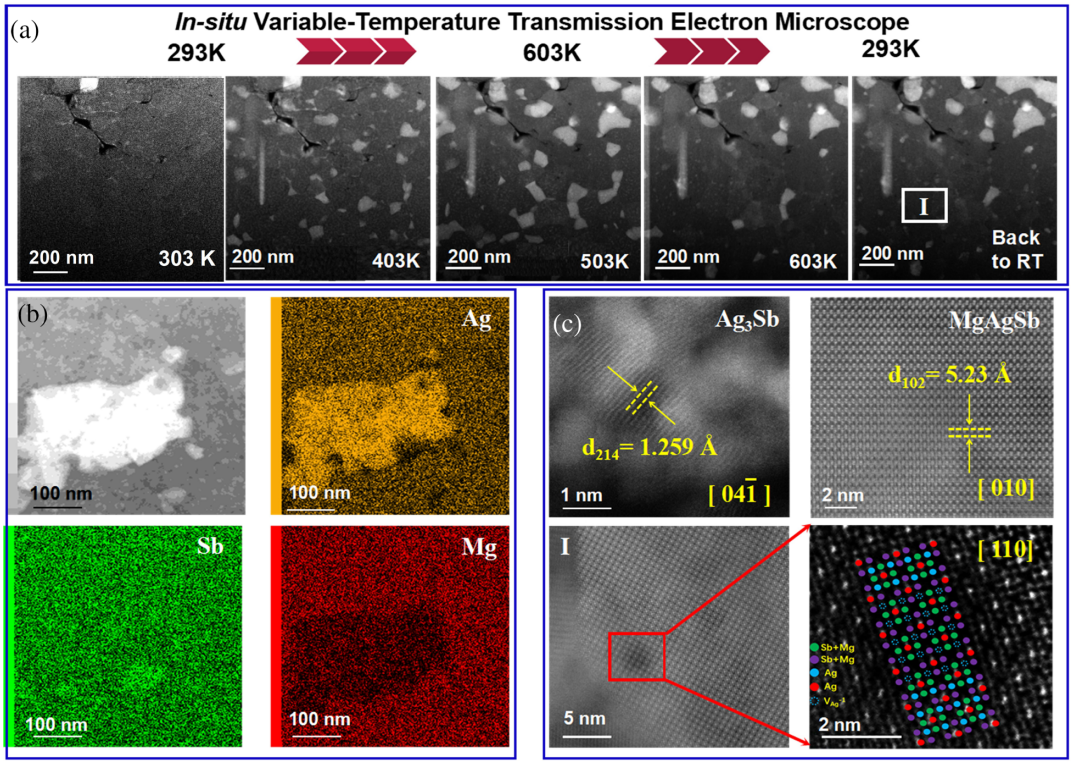

FIG. 3. *In situ* transmission electron microscope results. (a) High-angle annular dark-field images of a focused-ion-beam prepared MgAgSb sample recorded while heating from room temperature (RT) to 603 K and subsequently cooling back to RT. (b) Energy-dispersive x-ray spectroscopy (EDS) map showing the distribution of the precipitations that form during annealing. (c) HAADF images of the annealed MgAgSb sample taken along several crystallographic directions at RT. The lattice planes of Ag_3Sb precipitate and Ag vacancies in the MgAgSb matrix are prominently visible. Enlarged insets highlight individual Ag atoms (solid blue and red circles) and the accompanying vacancies (dotted blue circle).

vacancies. Once liberated, Ag ions diffuse swiftly through the MgAgSb crystal lattice and precipitate on the sample surface [26,39]. Ionic diffusion in solid materials is governed by $D = D_0 e^{-Q/\mathrm{RT}}$, where D is the diffusion coefficient, D_0 is the diffusion constant, and Q is the diffusion activation energy [26]. For FIB-prepared samples, the reduced thickness results in fewer atomic layers and shorter diffusion distances, promoting the longitudinal diffusion and migration of Ag atoms [40]. To preserve electrical (charge) neutrality within the MgAgSb crystal, Sb also precipitates, ultimately forming Ag_3Sb on the sample surface. This process does not markedly alter the material properties of the crystal. However, bulk samples exhibit different behavior, as demonstrated by the EDS analysis of annealed MgAgSb shown in Fig. S2 [27]. Two different regions in the annealed MgAgSb sample were chosen for scanning. At low magnification (Figs. S2a and S2c) [27], no obvious segregation is visible, and the elemental distribution appears uniform. However, a high-magnification view (Fig. S2b) reveals local Ag enrichment [27]. The elemental ratio analysis of the magnified region II (Fig. S2d) shows that the Ag concentration is substantially higher than that of Sb and Mg [27]. The results confirm that diffusion is limited in bulk samples: only trace amounts of Ag_3Sb precipitates are detected, and they do not affect the dominant phase and the TE performance of the bulk sample. *In situ* TEM images confirm the existence of trace Ag_3Sb precipitates. Notwithstanding this observation, the MgAgSb sample remains phase pure. This is consistent with the nonstoichiometric nature of MgAgSb, which is both kinetically and thermodynamically stable (as shown in Fig. S6) [22,27].

High-angle annular dark-field (HAADF) scanning transmission electron microscopy (STEM) imaging [Fig. 3(c)] further reveals polycrystalline Ag_3Sb precipitates embedded in the MgAgSb matrix, [27] as well asatomic-scale Ag vacancies within the MgAgSb matrix observed along the [110] direction. Differently colored dots in the HAADF image correspond to distinct atomic species. Specifically, these include five Ag atoms (red dots) and two Ag atoms (blue dots) within a single unit cell, as well as the overlapping projections of two Mg and two Sb atoms (green dots), and the overlapping projection of one Mg and one Sb atom (purple dots). These direct observations provide clear evidence that Ag migration and the formation of vacancies are responsible for the increase in hole concentration.

On the basis of the elevated carrier concentration, the electrical transport properties of annealed α-MgAgSb are improved compared with those of the as-synthesized MgAgSb. The TE properties of the as-synthesized and annealed samples are summarized in Fig. 4. As shown in Fig. 4(a), the room-temperature (303 K) carrier concentrations of α-MgAgSb annealed at different temperatures (373, 473, 573, 583, and 593 K) are presented. The results show that annealing above the phase transition temperature (583 K) induced a sharp increase in carrier concentration from 4.2×10^{19} to 1.3×10^{20} cm^{-3}, which is attributed to the formation of Ag vacancies. A pronounced increase in carrier concentration is obtained only when the annealing temperature exceeds the phase transition temperature. Despite the higher carrier concentration, the mobility decreased only slightly, which is attributed to improved crystallinity in the annealed sample (Fig. S3) and enhanced valley degeneracy that mitigates ionized impurity scattering [27]. The carrier mobility (μ) of α-MgAgSb was theoretically calculated using the single parabolic band (SPB) model. As shown in Fig. S7 [27], a comparison between the mobility calculated under high and low degeneracy band approximations reveals that the transport behavior of the as-grown sample agrees better with the low-degeneracy approximation. The mobility is primarily limited by the combined effects of acoustic phonon, grain boundary, ionized impurity, and point defect scattering, which is consistent with the behavior observed in annealed MgAgSb. Because of its high density of states (DOS) and number of valleys (N_V), the annealed sample maintains a high mobility even at a high carrier concentration. As a result, the electrical resistivity of MgAgSb decreases significantly after annealing [Fig. 4(b)], reaching as low as 10 $\mu\Omega \cdot \mathrm{m}$ at room temperature. As a reference, $MgAg_{0.97}Sb$ also exhibited a decrease in resistivity similar to that of the stoichiometric MgAgSb sample. With increasing temperature, the bipolar effect occurs at 423 K, which is higher than that in the as-synthesized MgAgSb sample due to the increased carrier concentration. When the temperature exceeded 423 K, the resistivity decreases with increasing temperature because electron-phonon interaction dominates the carrier transport. The Seebeck coefficient decreased with rising carrier concentration [Fig. 4(c)], in accordance with the relationship $S \propto n^{-2/3}$. For the annealed samples, the Seebeck coefficient increased from 180 $\mu\mathrm{V} \cdot \mathrm{K}^{-1}$ to a maximum of 203 $\mu\mathrm{V} \cdot \mathrm{K}^{-1}$ at 423 K, beyond which it declined due to the bipolar effect—a trend consistent with the resistivity behavior. The Seebeck coefficient retains a high absolute value owing to an increased DOS effective mass m^*. Fitting the Seebeck coefficient as a function of carrier concentration using the single parabolic band (SPB) model yields $m^* \approx 3.0 m_e$ for the annealed sample, exceeding previously reported values $\sim$2.3 m_e and 1.9 m_e [5,18], which correspond to the as-synthesized MgAgSb sample and earlier reports [5,17–20,30–32,41,42]. The enhancement of m^* further confirm the contribution of multivalley transport [Fig. 4(d)]. The improved electrical transport leads to a very high power factor, which increased from 23.5 to 30.3 $\mu\mathrm{W} \cdot \mathrm{cm}^{-1} \cdot \mathrm{K}^{-2}$ at room temperature, with an average value exceeding 30 $\mu\mathrm{W} \cdot \mathrm{cm}^{-1} \cdot \mathrm{K}^{-2}$ across 300–573 K [Fig. 4(e)]. For comparison, the power factor of the $MgAg_{0.97}Sb$ sample also increases relative to that of the

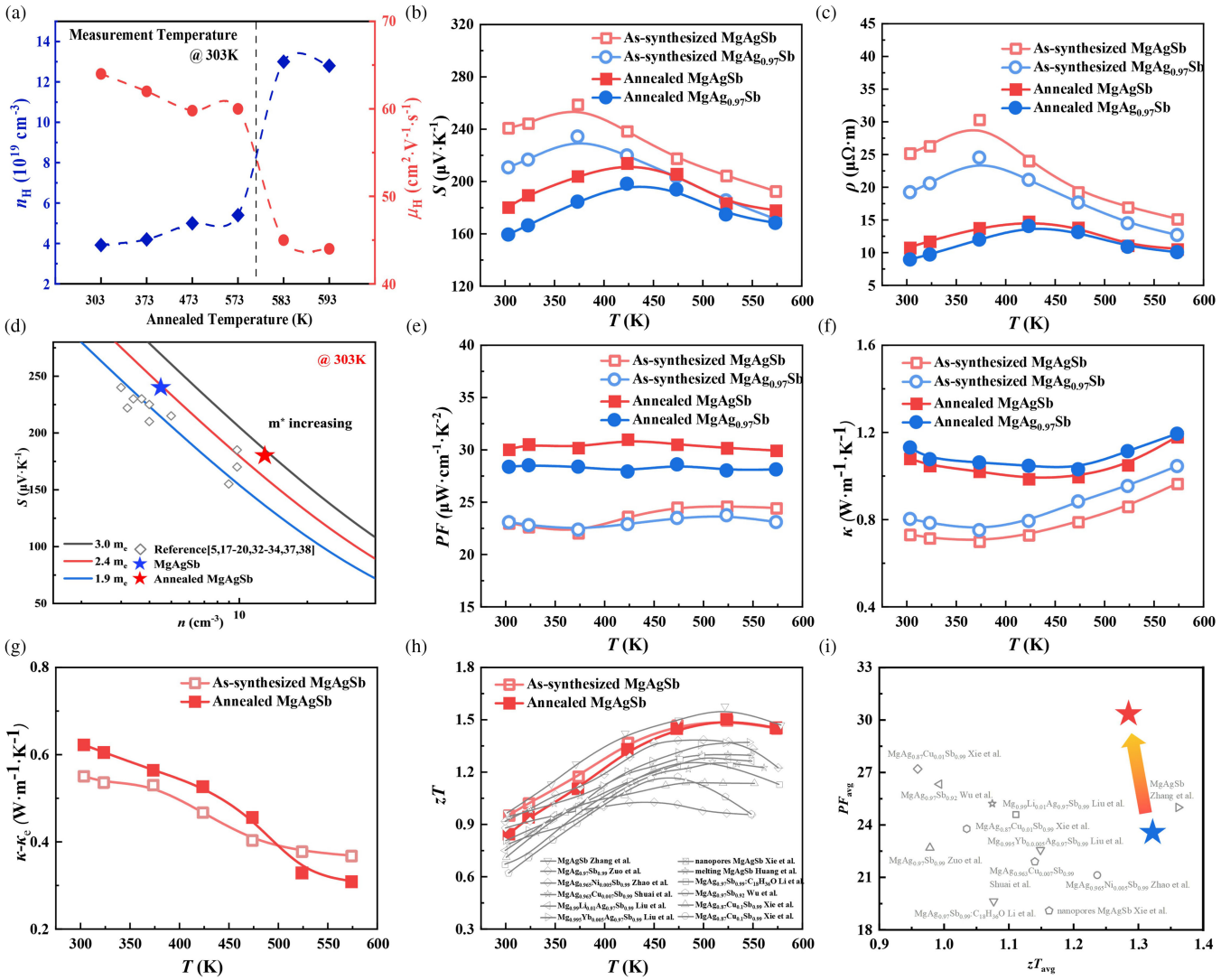

FIG. 4. The TE performance of the as-synthesized and the annealed MgAgSb samples. (a) The carrier concentration and mobility of MgAgSb at different annealed temperatures. (b) The comparison of the temperature-dependent Seebeck coefficient. (c) Resistivity of the as-synthesized $MgAg_{0.97}Sb$ and MgAgSb. (d) Carrier concentration dependence of Seebeck coefficient at 303 K, the lines are calculated by a single parabolic band model with specific effective masses [5,17–20,30–32,41,42]. (e) The comparison of the temperature-dependent power factor, (f) thermal conductivity of the as-synthesized $MgAg_{0.97}Sb$ and MgAgSb. (g) The comparison of the temperature-dependent lattice thermal conductivity of the as-synthesized and annealed MgAgSb. (h) The comparison of zT values of MgAgSb-based materials from 300 to 573 K [5,14–19,29–33]. (i) The average power factor and zT of MgAgSb-based materials from 300 to 573 K [5,14–19,29–33].

as-synthesized sample. It indicates that the increasing band degeneracy leads to an enhancement in electrical transport properties. This represents the highest power factor reported to date for α-MgAgSb-based materials, marking a critical step toward compatibility with high-performance n-type Mg_3Sb_2-based compounds.

To address the limitations of the SPB model in complex, high-carrier-concentration systems, we employed first-principles band-occupation calculations to directly demonstrate how Fermi-level shifts activate specific transport valleys (Fig. S8) [27]. In this plot, the color scale represents hole occupation: values close to 0 indicate negligible hole occupation, whereas values close to 2 indicate a high degree of hole occupation. From the band structures near the Fermi level, the Ag-vacancy case exhibits flatter bands and a larger number of states in a narrow energy range, which is consistent with an increased density-of-states effective mass. This mainly reflects the contribution of the larger effective mass to the power factor enhancement. More importantly, the band occupation analysis provides more direct evidence for multivalley transport activation. In pristine α-MgAgSb, the valence bands below the Fermi level are nearly fully occupied, and the hole occupation around the valence band edge is therefore

negligible. In contrast, in the Ag-vacancy model, clear hole occupation appears at the valence band edge. This hole occupation is not confined to a single valence band maximum, but is distributed among the secondary and third valence band maxima at different k points. This indicates that, after the introduction of Ag vacancies, holes populate multiple valence band valleys near the band edge. Therefore, the improvement in power factor can be understood from two effects: the flatter bands contribute to a larger effective mass and higher density of states, while the occupation of multiple valleys demonstrates increased valley participation in transport.

Although the total thermal conductivity increases slightly after annealing, from ~1.05 to ~1.19 $W \cdot m^{-1} \cdot K^{-1}$ for the annealed MgAgSb sample over the measured temperature range [Fig. 4(f)], this increase is primarily owing to the enhanced electronic thermal conductivity dictated by the Wiedemann-Franz law [43,44].

The lattice thermal conductivity of the annealed MgAgSb sample exhibited a minor increase compared with that of the as-synthesized sample at lower temperatures (below 450 K) and remained low overall [Fig. 4(g)], which is attributed to the formation of metallic Ag_3Sb precipitates that provide additional pathways for phonon transport. The annealing treatment significantly increases the concentration of Ag-vacancy defects in MgAgSb samples. At temperature above 450 K, the stronger phonon scattering due to more defects led to a decrease in lattice thermal conductivity, especially in annealed MgAgSb.

First-principles calculations were employed to assess the impact of microstructural features on lattice thermal transport in α-MgAgSb ($\kappa_x = \kappa_y = 0.537$, $\kappa_z = 0.692$ $W \cdot m^{-1} \cdot K^{-1}$). Analysis of the cumulative κ as a function of phonon MFP (Fig. S9) shows that ~90% of the thermal conductivity arises from phonons with submicrometer MFPs (~0.45 μm in-plane, ~1.1 μm out-of-plane) [27]. The experimentally observed Ag_3Sb precipitates after annealing are separated by micrometer-scale distances, with most interprecipitate spacings exceeding ~500 nm [Fig. 3(a)]. This length scale is significantly larger than the characteristic phonon MFPs that dominate lattice thermal conductivity.

In terms of carrier transport, the micrometer-scale separation of Ag_3Sb precipitates precludes the formation of a dense scattering network, making long-range carrier scattering unlikely. Conversely, because Ag_3Sb is metallic, its precipitation results in a modest increase in the lattice thermal conductivity.

Because of the increase in thermal conductivity, the room-temperature zT of the annealed MgAgSb sample decreased slightly from 0.95 to 0.87. Nevertheless, the significantly enhanced power factor led to improved zT values in the high-temperature region. As illustrated in Fig. 4(h), the annealed MgAgSb sample achieved excellent zT values compared with most previously reported data in the literature [5,14–19,29–33].

The significant gain in power factor outweighs the moderate increase in thermal conductivity, resulting in a high average zT of 1.30, only marginally lower than that of the as-synthesized sample ($zT_{avg} = 1.32$) over the temperature range from 300 to 573 K, as illustrated in Fig. 4(i). More notably, the annealed MgAgSb sample achieves a record-high average power factor in this temperature range, surpassing all previously reported values for MgAgSb-based materials [5,14–19,29–33].

We have added several control experiments to confirm that the observed effect is not merely a result of simple heat treatment, but that annealing within the β-phase temperature region is responsible for the enhancement of carrier concentration. As shown in Fig. S10 [27], annealing was performed at 563, 573, 583, and 593 K. It can be seen that no obvious changes in TE parameters occurred at annealing temperatures below 583 K (α-β phase transition temperature). Furthermore, the reproducibility of this annealing strategy was confirmed using samples annealed at 588, 593, 598, and 603 K, all of which exhibited consistently enhanced power factors and TE performance when annealed above the phase transition temperature. The results indicate that the enhancement of carrier concentration is achieved not by general heat treatment, but by annealing in the β phase.

In addition to the above, we performed supplementary experiments with different cooling rates across the phase transition temperature (593 K), including slow cooling at a controlled rate, natural cooling in the furnace, and rapid cooling by quenching. The results are shown in the Fig. S11 [27]. As seen, changing the cooling rate has little effect on slowly cooled and naturally cooled samples. In contrast, the rapidly cooled (quenched) samples exhibit a significantly lower Seebeck coefficient and electrical resistivity. Carrier concentration measurements of these three samples further show that the quenched sample has a much higher carrier concentration. These results indicated that Ag vacancies can reequilibrate in the α phase during cooling, whereas rapid cooling preserves a larger number of Ag vacancies, resulting in a higher carrier concentration (Table S4 [27]). Consequently, the final thermoelectric zT of the quenched sample is slightly lower than that of the slowly cooled samples.

To the best of our knowledge, this is the first report of using a phase-transition-based annealing process to tune the carrier concentration and enhance TE performance without chemical doping. This strategy ensures that both high conversion efficiency and high output power can be simultaneously achieved in device applications.

To evaluate the practical performance, a single-leg module ($3.14 \times 3.00 \times 7.00$ mm^3) was fabricated. Among various electrode materials (Ag, Co, $MgAgMn_{0.01}$, MgCuSb,

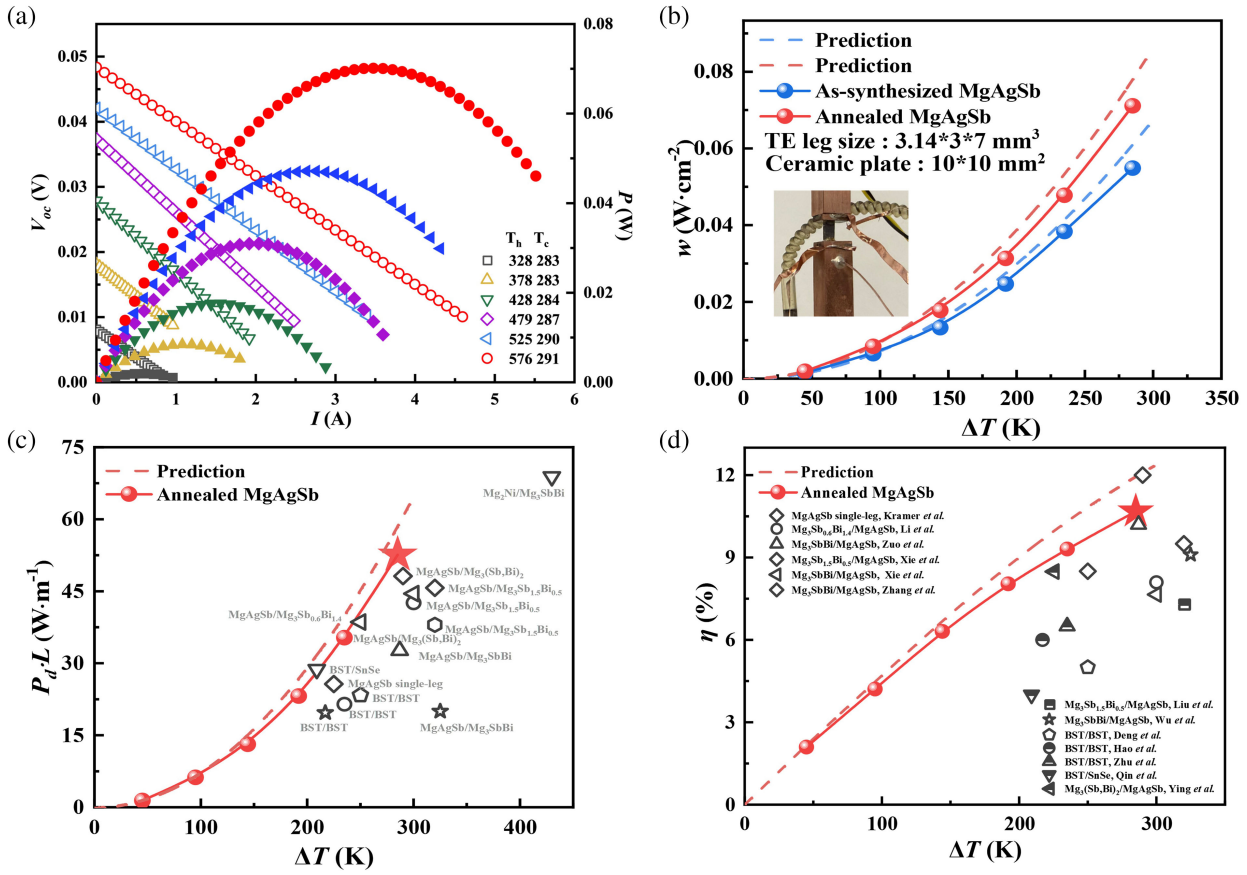

FIG. 5. The performance of power generation and TE cooling modules. (a) Output voltage-output power evolutions versus current at different temperature gradients of the annealed single-leg MgAgSb module. (b) The calculated and experimental power density of the single leg as-synthesized and the annealed MgAgSb modules. (c) The Comparison between the product of the reduced power density and the leg length of the annealed MgAgSb single leg module with other MgAgSb power generation devices [5,14,16,29,32,34–38]. (d) The comparison of the maximum TE conversion efficiency of the annealed MgAgSb device at different temperatures versus other materials [5,14,16,29,32,34–38].

and Sb) reported for MgAgSb [5,14–16,29,45], Ag was selected and sintered onto the MgAgSb pellets. Although prolonged annealing or a large interfacial area can increase contact resistivity, as reported in our previous work [46], the contact resistivity at the Ag/MgAgSb interface in this work increased only moderately from 11.3 to 17.9 $\mu\Omega \cdot \mathrm{cm}^2$ after annealing, as shown in Fig. S5 [27]. We compared the EDS results of the Ag/MgAgSb contact layer before and after heat treatment (Figs. S12–16) [27], which illustrate the effects of different annealing times (20, 40, 60, and 100 h). After 100 h of annealing, microcracks can be observed in the Ag-MgAgSb contact layer. The results show that interfacial diffusion increases with annealing time, leading to gradual interfacial degradation. In contrast, short-time annealing has a minor effect on the interface in this work.

The reduced cross section and rapid annealing process help minimize interfacial degradation. As shown in Fig. 5, the power generation performance was evaluated under various temperature gradients. Figure 5(a) demonstrated that the output voltage varies linearly with current, with the intercept and slope representing the open-circuit voltage (V_{oc}) and internal resistance (R_{in}), respectively. Both parameters correlated with the Seebeck coefficient and electrical resistance of the MgAgSb leg under different ΔT. The output power (P_{out}), calculated from the voltage and current, initially increases and then decreases as the current increases, reaching a maximum of ~0.071 W at $\Delta T = 285$ K, as shown in Fig. 5(b). The output power is in good agreement with the theoretical value at lower temperatures, but the discrepancies increased at higher temperatures due to the radiation losses from the ceramic plate and the contact resistance between the module and the heat source, resulting in the actual ΔT being lower than the set ΔT. Even so, the annealed sample exhibits a 30% improvement in P_{max} over the as-synthesized sample (0.054 W). To fairly evaluate the output capability, we use the reduced specific power density $P_d \times L$, where $P_d = P_{out}/S_{(n+p)}$ represents the output power per cross-section area of a single n/p leg. As shown in Fig. 5(c), the annealed MgAgSb sample achieved a reduced specific power density

of 52.6 $W \cdot m^{-1}$ at $\Delta T = 285$ K, surpassing most previously reported devices [5,14,16,29,32,34–38]. This high output power density directly results from the enhanced power factor of the annealed MgAgSb material [47,48].

Subsequently, cycling tests were conducted on both the MgAgSb thermoelectric material and the single leg, as shown in Fig. S17 [27]. The results show that the presence of these precipitates does not lead to obvious degradation in the cycling performance of the thermoelectric material itself. We then measured the open-circuit voltage (V_{oc}) at 573 K and the internal resistance (R_{in}) of the device at 303 K. While V_{oc} remained stable, R_{in} gradually increased with the number of cycles (after 120 h). This increase is primarily attributed to the evolution of the Ag electrode/MgAgSb interface during long-term cycling. Although the total internal resistance of the device increases, the change remains below 10%, resulting in no significant impact on the overall device performance.

Finally, the power generation efficiency reached a maximum conversion efficiency (η) of ~10.7% at $\Delta T =$ 285 K [Fig. 5(d)]. The annealed module demonstrated a high conversion efficiency in the near-room-temperature region. The combination of high output power and high efficiency makes annealed MgAgSb a promising candidate to replace Bi_2Te_3-based materials in near-room-temperature power generation applications.

In summary, we have developed a rapid annealing strategy that utilizes the $\alpha - \beta$ phase transition of α- MgAgSb to deliberately introduce Ag vacancies—the dominant point defects in this system. The increased Ag-vacancy concentration effectively raises the hole carrier density, as confirmed by *in situ* temperature-dependent TEM and PND. Theoretical calculations indicate that the elevated carrier concentration activates multivalley transport, leading to a remarkable power factor of 30 $\mu W \cdot cm^{-1} \cdot K^{-2}$ at room temperature—up from 23.7 $\mu W \cdot cm^{-1} \cdot K^{-2}$ before annealing—and an average value of 31 $\mu W \cdot cm^{-1} \cdot K^{-2}$ over the operating temperature range, the highest reported to date for MgAgSb-based materials. The optimized sample achieves a room-temperature zT of 0.85 and an average zT of 1.30 from 303 to 573 K. A single-leg module exhibits a conversion efficiency of 10.7% and an output power of 0.071 W at $\Delta T = 285$ K, demonstrating high efficiency and power density in the near-room-temperature regime. This work not only substantially advances the TE performance of MgAgSb, but also presents a generalizable, doping-free route for carrier concentration optimization via phase transformation, which is potentially applicable to other multiphase functional electronic material systems.

The authors acknowledge the funding support of the Beijing Science and Technology Research Plan (Z231100006623002), and the National Natural Science Foundation of China (52576073). The authors thank the China Spallation Neutron Source for the granted beam time on the General-Purpose Powder Diffractometer [49] and the beamline scientist Dr. Lunhua He for her assistance. The numerical computation is completed on the HPC Platform of Huazhong University of Science and Technology and the Hefei Advanced Computing Center.

DATA AVAILABILITY

The data are not publicly available. The data are available from the authors upon reasonable request.

APPENDIX: METHODS

1. Materials synthesis and annealing process

As-synthesized MgAgSb samples were synthesized by two-step ball milling. High-purity Mg turnings (99.9%) and Ag particles (99.99%) were weighed according to the atomic ratio of 1:1 into a stainless-steel jar with tungsten carbide balls in a glove box full of Ar, and then ball milled in a high-energy ball milling machine for 10 h. Then the MgAg powder after ball milling and Sb shots (99.99%) were mixed in the ball milling jar, and ball milled 10 h. The MgAgSb powder was packed into a graphite mold with a diameter of 12.7 mm and sintered at 573 K for 5 min at a pressure of 80 Mpa. The obtained MgAgSb pellet was put into a ZrO_2 crucible. The crucible was surrounded by quartz wadding placed above and below, and the entire assembly was placed inside the quartz tube. The tube was vertically placed in a heating furnace. First, the temperature was raised to 563 K at the heating rate of 1 $K \cdot min^{-1}$, and then the temperature was raised to 623 K slowly at the heating rate of 0.1 $K \cdot min^{-1}$ and kept at 623 K for 30 min. Then, it was cooled to 563 K at a cooling rate of 1 $K \cdot min^{-1}$, and finally cooled down to room temperature.

2. Crystal and microscopic characterizations

The powder neutron diffraction was tested at the Dongguan spallation neutron source, the spectrometer used is GPPD. Both the results of XRD and neutron diffraction results were refined using GSAS II. The lattice parameters of all samples were obtained by the Fullprof program. The microstructure of the MgAgSb sample was carried out on scanning electron microscope, and energy dispersive spectroscopy analysis was obtained on FEI TALOS F200A. High-quality thin-cross-sectional samples for TEM were prepared by using focused ion beam (FIB, Helios 600i, FEI). The *bright-field* (BF) TEM, *in situ* TEM, EDS mapping, and high-angle annular dark-field images were acquired by a JEOL JEM-ARM200F NEOARM. And the FIB samples were placed on an *in situ* heating holder for temperature control. The HAADF images, the SAED patterns, and the EELS spectrum were achieved on a JEOL ARM200F TEM equipped with a double spherical

aberration corrector at 200 kV. The SAED patterns were acquired at an exposure time of 3s and an aperture of ~150 nm. The HAADF images were collected at acceptance angles of 90 ~ 370 mrad.

3. Measurement of thermoelectric properties

The α-MgAgSb pellets were cut into bars with a dimension of $3 \times 2.5 \times 9$ mm^3, and the electrical and Seebeck coefficient were measured along the in-plane direction by LSR apparatus (Linseis, LSR-3, Germany). The sintered samples have a diameter of 12.7 mm and a thickness of 2.5 mm. Thermal diffusivity D were measured by LFA 1000 (Linseis, Germany) for all samples, and the density ρ of different pellets was measured by Archimedes drainage method. The heat capacity C_p was estimated according to the Dulong-Petit law. Based on the above parameters, the thermal conductivity can be calculated by using this formula:

$$\kappa = \rho C_p D. \tag{A1}$$

The measurement uncertainties are 3%, 5%, and 6% for electrical resistivity, Seebeck coefficient, and thermal diffusivity, respectively, which yield an error in zT of ~20%.

4. Simulation of the thermoelectric transport mechanism

According to the SPB model [50]

$$n = \frac{4\pi(2m^* k_B T)^{\frac{3}{2}}}{h^3} F_{\lambda+\frac{1}{2}}(\eta), \tag{A2}$$

$$S = -\frac{k_B}{e}\left(\frac{(2+\lambda)F_{\lambda+1}(\eta)}{(1+\lambda)F_\lambda(\eta)} - \eta\right), \tag{A3}$$

$$L = -\frac{{k_B}^2}{e^2}\left[\frac{(3+\lambda)(1+\lambda)F_\lambda(\eta)F_{\lambda+2}(\eta)}{(1+\lambda)^2 F_\lambda(\eta)^2} - \frac{(2+\lambda)^2 F_{\lambda+1}(\eta)^2}{(1+\lambda)^2 F_\lambda(\eta)^2}\right], \tag{A4}$$

$$F_i(\eta) = \int_0^\infty \frac{x^i dx}{1 + e^{x-\eta}}. \tag{A5}$$

The k_B, e, and h are the Boltzmann constant, electron charge, and the Planck constant, respectively. λ is the scattering factor, $m*$ is the density of state effective mass, η is the reduced Fermi level, x is the reduced carrier energy, and $F_i(\eta)$ is the Fermi-Dirac integral. Both the acoustic phonon scattering and alloy scattering give $\lambda = 0$. And the mobility can be depicted as

$$\frac{1}{\mu} = \frac{1}{\mu_{\mathrm{AC}}} + \frac{1}{\mu_{\mathrm{ION}}} + \frac{1}{\mu_{\mathrm{GB}}} + \frac{1}{\mu_{\mathrm{PD}}}. \tag{A6}$$

These correspond to acoustic phonon scattering, ionic scattering, grain boundary scattering, and point defect scattering, respectively. The scattering of different mechanisms is given by literature [51,52]

$$\mu_{\mathrm{AC}} = \frac{2^{\frac{1}{2}}\pi e h^4}{3(k_B T)^{\frac{3}{2}}} \frac{{\vartheta_l}^2 d}{{E_{\mathrm{def}}}^2 (m^*)^{\frac{3}{2}} m_I^*} \frac{F_0(\eta)}{F_{\frac{1}{2}}(\eta)}, \tag{A7}$$

$$\mu_{\mathrm{ION}} = \frac{64\pi^{\frac{1}{2}}\varepsilon_0^2 \varepsilon_S^2 (2k_B T)^{\frac{3}{2}} \pi e h^4}{N_I q^3 m^{*\frac{1}{2}} \ln\left[1 + \left(\frac{12\pi\varepsilon_0\varepsilon_S k_B T}{q^2 N_I^{\frac{1}{3}}}\right)^2\right]}, \tag{A8}$$

$$\mu_{\mathrm{GB}} = \mathrm{De}\left(\frac{1}{2\pi m^* k_B T}\right)^{\frac{1}{2}} \exp\left(-\frac{E_b}{k_B T}\right), \tag{A9}$$

$$\mu_{\mathrm{PD}} = \frac{\pi^2 m^* q^3}{10\varepsilon_0 \varepsilon_S N_N h^3}, \tag{A10}$$

where ϑ_l is the velocity of longitudinal sound waves, d is the density, E_{def} the deformation potential, ε the dielectric constant, N_I the ionized impurity concentration, D the grain size, E_b the potential barrier of the boundary, and N_N the neutral impurity concentration.

5. The calculation of vacancy formation energy using density functional theory

The first-principles calculations were carried out with Vienna *ab initio* simulation package (VASP) [53] using Perdew Burke-Ernzerhof (PBE) exchange-correlation functional pseudopotentials including the generalized gradient approximation (GGA) [54]. Variable-cell relaxations were performed until the convergence criteria for energy and the largest residual force fell below 10^{-8} eV and 10^{-6} eV/Å, respectively, giving optimized lattice constants $a = 9.268$, $b = 9.268$, and $c = 12.765$ Å for α-MgAgSb, and $a = 4.432$, $b = 4.432$, and $c = 7.415$ Å for β-MgAgSb. To facilitate a direct comparison of the defect formation energies and carrier properties between the two phases, a $2 \times 2 \times 2$ supercell of β- MgAgSb was constructed, ensuring that both α-MgAgSb and β-MgAgSb contain the same number of 48 atoms in their simulation cells. Self-consistent fields were converged to 10^{-8} eV with a $9 \times 9 \times 6$ k mesh and a 400 eV plane-wave cutoff. To investigate the effects of point defects on the properties of MgAgSb, defect supercells were constructed based on the 48-atom primitive cell. For α-MgAgSb, three inequivalent Ag sites were considered, while for β-MgAgSb, two distinct Ag sites were modeled to generate the corresponding defect configurations.

For the non-self-consistent electronic band structure calculations, the modified Becke-Johnson (mBJ) potential was employed to accurately determine the band gaps

[55,56]. Electron localization function (ELF) was performed for α-MgAgSb and β-MgAgSb, which is defined as [57]

$$\mathrm{ELF} = \left\{1 + \left[\frac{D_P(r)}{D_H(r)}\right]^2\right\}^{-1}, \tag{A11}$$

where $D_P(r)$ denotes the Pauli kinetic energy density, and $D_H(r)$ represents the kinetic energy density of a homogeneous electron gas with the same local electron density.

For phonon properties, the second-order force constants were obtained using the finite displacement method with a $2 \times 2 \times 2$ supercell based on the primitive cell [58]. With the second-order force constant, the phonon dispersion relations were then calculated using a $12 \times 12 \times 12$ mesh.

The defect formation energy ΔH is defined as

$$\Delta H(D, q, E_F) = E(D, q) - E(\mathrm{perfect}) + \sum n_i \mu_i + q(E_{\mathrm{VBM}} + E_F), \tag{A12}$$

Where $E(D, q)$ is the total energy of the supercell containing a defect in charge state q, $E(\mathrm{perfect})$ denotes the total energy of the corresponding pristine supercell. The term n_i represents the number of atoms of type i added to ($n_\mathrm{i} < 0$) or removed from ($n_\mathrm{i} > 0$) the system, and μ_i is the chemical potential of species i, E_F is the Fermi level referenced to the valence-band maximum (EVBM).

As a result, the formation energies of defects at the three Ag sites (Ag_1, Ag_2, Ag_3) in the α-phase MgAgSb are all higher than those at the Ag_1 and Ag_2 sites in the β phase. Among these, the formation energy of the Ag_1 defect is the lowest, which is consistent with our neutron results. The specific results are presented in Table S1 [27].

6. The fabrication and characterization of the thermoelectric performance of the α-MgAgSb device

In this work, the Ag electrode was still chosen to be the contact layer of MgAgSb. The SPS-ed Ag-MgAgSb pellet was cut into a thermoelectric leg with a dimension of $3.14 \times 3 \times 7$ mm^3. And the TE leg undergoes the annealed process, and then was fabricated the single-leg TE module. The electrical contact of the Ag-MgAgSb interface in as-synthesized and annealed samples was measured by the four-probe technique, and the results were shown in Fig. S5 [27]. The contact resistivity slightly increased in the annealed sample, with little impact on the device's performance. As-synthesized and annealed thermoelectric legs were tested for power generation measurement by Mini-PEMs (ADVANCE RIKO, Japan). The hot side temperature T_h of the module was controlled by a heater, and the cold-side temperature T_c was controlled by the flowing water. Both T_h and T_c were measured by thermocouples of the Mini-PEM. The output power (P) and cold-side heat flow (Q_c) were recorded using the Mini-PEM. Therefore, the power-generation efficiency was calculated using the equation.

$$\eta = \frac{P}{Q_\mathrm{in}} = \frac{P}{P + Q_\mathrm{out}}. \tag{A13}$$

The prediction of the thermoelectric efficiency is based on the formula

$$\eta = \frac{\Delta T}{T_h} \frac{\sqrt{1 + \overline{zT}} - 1}{\sqrt{1 + \overline{zT}} + \frac{T_c}{T_h}}. \tag{A14}$$

Since z is temperature-dependent, in order to avoid overestimation, the predicted output power density w can be calculated by the following formula:

$$w = \frac{(T_h - T_c)^2}{4L} \overline{\mathrm{PF}}. \tag{A15}$$

where ($\overline{\mathrm{PF}}$) and L are the average power factor and the single-leg length, respectively. The length of the two legs is all 7 mm.

[1] G. Jeffrey Snyder and Eric S. Toberer, *Complex thermoelectric materials*, Nat. Mater. **7**, 105 (2008).

[2] Jian He and Terry M. Tritt, *Advances in thermoelectric materials research: Looking back, and moving forward*, Science **357**, eaak9997 (2017).

[3] Jun Mao, Hangtian Zhu, Zhiwei Ding, Zihang Liu, Geethal Amila Gamage, Gang Chen, and Zhifeng Ren, *High thermoelectric cooling performance of n-type* Mg_3Bi_2*-based materials*, Science **365**, 495 (2019).

[4] Cheng Chang, Minghui Wu, Dongsheng He, Yanling Pei, Chaofeng Wu, Fangyuan Zhu, Yue Chen, Kedong Wang, Li Huang, Jing-feng Li, Jiaqing He, and Lidong Zhao, *3D charge, and 2D phonon transports leading to high out-of-plane ZT in n-type* SnSe *crystals*, Science **360**, 778 (2018).

[5] Xiaofan Zhang, Hangtian Zhu, Xuejuan Dong, Zhen Fan, Yuan Yao, Nan Chen, Jiawei Yang, Kaiwei Guo, Jiazheng Hao, Lunhua He, Guodong Li, and Huaizhou Zhao, *High-performance* $MgAgSb/Mg_3(Sb, Bi)_2$*-based thermoelectric with* $\eta = 12\%$ *at* $T \leq 583$ K, Joule **8**, 3324 (2024).

[6] Airan Li, Longquan Wang, Xinzhi Wu, Jiankang Li, Xinyuan Wang, Gang Wu, Zhao Hu, and Takao Mori, *Semiconductor-metal transition powers high-efficiency* MgAgSb *thermoelectrics*, Sci. Adv. **11**, eadx7115 (2025).

[7] Zhonglin Bu, Xinyue Zhang, Yixin Hu, Zhiwei Chen, Siqi Lin, Wen Li, Chong Xiao, and Yanzhong Pei, *A record thermoelectric efficiency in tellurium-free mudules for low-grade waste heat recovery*, Nat. Commun. **13**, 237 (2022).

[8] Qingyu Yan and Mercouri G. Kanatzidis, *High-performance thermoelectrics, and challenges for practical devices*, Nat. Mater. **21**, 503 (2022).

[9] Rigui Deng, Xianli Su, Shiqiang Hao, Zheng Zheng, Min Zhang, Hongyao Xie, Wei Liu, Yonggao Yan, Chris Wolverton, Ctirad Uher, Mercouri G. Kanatzidis, and

Xinfeng Tang, *High thermoelectric performance in* $Bi_{0.46}Sb_{1.54}Te_3$ *nanostructured with* ZnTe, Energy Environ. Sci. **11**, 1520 (2018).

[10] Bed Poudel, Qing Hao, Yi Ma, Yucheng Lan, Austin Minnich, Bo Yu, Xiao Yan, Dezhi Wang, Anderw Muto, Daryoosh Vashaee, XiaoYuan Chen, Junming Liu, Mildred S. Dresselhaus, Gang Chen, and Zhifeng Ren, *High-thermoelectric performance of nanostructured bismuth antimony telluride bulk alloys*, Science **320**, 634 (2008).

[11] Feng Hao, Pengfei Qiu, Yunshan Tang, Shengqiang Bai, Tong Xing, Hsu-Shen Chu, Qihao Zhang, Ping Liu, Tiansong Zhang, Dudi Ren, Jikun Chen, Xun Shi, and Lidong Chen, *High efficiency* Bi_2Te_3*-based materials, and devices for thermoelectric power generation between 100, and* 300 °C, Energy Environ. Sci. **9**, 3120 (2016).

[12] Pedersen, Hao Yin, Le Thanh Hung, and Bo Brummerstedt Iversen, *Discovery of high-performance low-cost n-type* Mg_3Sb_2*-based thermoelectric materials with multi-valley conduction bands*, Nat. Commun. **8**, 13901 (2016).

[13] Nan Chen, Hangtian Zhu, Guodong Li, Zhen Fan, Xiaofan Zhang, Jiawei Yang, Tianbo Lu, Qiulin Liu, Xiaowei Wu, Yuan Yao, Youguo Shi, and Huaizhou Zhao, *Improved figure of merit (z) at low temperature for superior thermoelectric cooling in* $Mg_3(Bi, Sb)_2$, Nat. Commun. **14**, 4932 (2023).

[14] Airan Li, Longquan Wang, Jiankang Li, Xinzhi Wu, and Takao Mori, *Self-optimized contact in air-robust thermoelectric junction towards long-lasting heat harvesting*, Nat. Commun. **16**, 1502 (2025).

[15] Liangjun Xie, Li Yin, Guyang Peng, Shaowei Song, Pingjun Ying, Songting Cai, Yuxin Sun, Wenjing Shi, Hao Wu, Nuo Qu, Fengkai Guo, Wei Cai, Haijun Wu, Qian Zhang, Kornelius Nielsch, Zhifeng Ren, Zihang Liu, and Jiehe Sui, *Screening strategy for developing thermoelectric interface materials*, Science **382**, 921 (2023).

[16] Xinzhi Wu, Yangjian Lin, Chengyan Liu, Yupeng Wang, Huan Li, Binghui Ge, and Weishu Liu, *A high performance eco-friendly* MgAgSb*-based thermoelectric power generation device near phase transition temperatures*, Energy Environ. Sci. **17**, 2879 (2024).

[17] Zihang Liu, Yumei Wang, Jun Mao, Huiyuan Geng, Jing Shuai, Yuanxu Wang, Ran He, Wei Cai, Jiehe Sui, and Zhifeng Ren, *Lithium doping to enhance thermoelectric performance of* MgAgSb *with weak electron-phonon coupling*, Adv. Energy Mater. **6**, 1502269 (2016).

[18] Jiehe Sui, Jing Shuai, Yucheng Lan, Yuan Liu, Ran He, Dezhi Wang, Qing Jie, and Zhifeng Ren, *Effect of* Cu *concentration on thermoelectric properties of nanostructured p-type* $MgAg_{0.97-x}Cu_xSb_{0.99}$, Acta Mater. **87**, 266 (2015).

[19] Airan Li, Longquan Wang, Jiankang Li, and Takao Mori, *Global softening to manipulate sound velocity for reliable high-performance* MgAgSb *thermoelectrics*, Energy Environ. Sci. **17**, 8810 (2024).

[20] Pingjun Ying, Xiaohua Liu, Chenguang Fu, Xianqiang Yue, Hanhui Xie, Xinbing Zhao, Wenqing Zhang, and Tiejun Zhu, *High performance* α-MgAgSb *thermoelectric materials for low temperature power generation*, Chem. Mater. **27**, 909 (2015).

[21] Zihang Liu, Huiyuan Geng, Jun Mao, Jing Shuai, Ran He, Chao Wang, Wei Cai, Jiehe Sui, and Zhifeng Ren, *Understanding, and manipulating the intrinsic point defect in* α-MgAgSb *for higher thermoelectric performance*, J. Mater. Chem. A **4**, 16834 (2016).

[22] Zhenzhen Feng, Jihua Zhang, Yuli Yan, Guangbiao Zhang, Chao Wang, Chenxiao Peng, Fengzhu Ren, Yuanxu Wang, and Zhenxiang Cheng, Ag − Mg *antisitee defect induced high thermoelectric performance of* α-MgAgSb, Sci. Rep. **7**, 2572 (2017).

[23] Alex Zevalkink, David M. Smiadak, Jeff L. Blackburn, Andrew J. Ferguson, Michael L. Chabinyc, Olivier Delaire, Jian Wang, Kirill Kovnir, Joshua Martin, Laura T. Schelhas, Taylor D. Sparks, Stephen D. Kang, Maxwell T. Dylla, G. Jeffery Snyder, Brenden R. Oriz, and Eric S. Toberer, *A practical field guide to thermoelectrics: Fundamentals, synthesis, and characterization*, Appl. Phys. Rev. **5**, 021303 (2018).

[24] Dandan Li, Huaizhou Zhao, Shanming Li, Beipei Wei, Jing Shuai, Chenglong Shi, Xuekui Xi, Peijie Sun, Sheng Meng, Lin Gu, Zhifeng Ren, and Xiaolong Chen, *Atomic disorders induced by silver, and magnesium ion migrations favor high thermoelectric performance in* α-MgAgSb*-based materials*, Adv. Funct. Mater. **25**, 6478 (2015).

[25] M. J. Kirkham, A. M. dos Santos, C. J. Rawn, E. Lara-Curzio, J. W. Sharp, and A. J. Thompson, *Ab-initio determination of crystal structures of the thermoelectric material* MgAgSb, Phys. Rev. B **85**, 144120 (2012).

[26] Hyun Seok Oh, Sang Jun Kim, Khorgolkhuu Odbadakh, Wook Ha Ryu, Kook Noh Yoon, Sai Mu, Fritz Körmann, Yuji Ikeda, Cemal Cem Tasan, Dierk Raabe, Takeshi Egami, and Eun Soo Park, *Engineering atomic-level complexity in high-entropy, and complex concentrated alloys*, Nat. Commun. **10**, 2090 (2019).

[27] See Supplemental Material at http://link.aps.org/supplemental/10.1103/gqjx-6kqr for figures and tables containing supporting characterization, calculation, and experimental results, which includes Figs. S1–S17, and Tables S1–S4, Ref. [22].

[28] Kaiwei Guo, Xiaofan Zhang, Zhen Fan, Yi Wang, Jiawei Yang, Hangtian Zhu, Jing Chen, Qi Zhao, Zhiliang Li, Shufang Wang, Qinghua Zhang, Yuan Yao, Lunhua He, and Huaizhou Zhao, *Rational manipulation of Ag vacancies for latiice plainification, and superior thermoelectric performance in* α-MgAgSb, Chem. Eng. J. **507**, 160515 (2025).

[29] Wusheng Zuo, Hongyi Chen, Ziyi Yu, Yuntian Fu, Xin Ai, Yanxiao Cheng, Meng Jiang, Shun Wan, Zhengqian Fu, Rui Liu, Guofeng Cheng, Rui Xu, Lianjun Wang, Fangfang Xu, Qihao Zhang, Denys Makarov, and Wan Jiang, *Atomic-scale interface strengthening unlocks efficient, and durable* Mg*-based thermoelectric devices*, Nat. Mater. **24**, 735 (2025).

[30] Liangjun Xie, Guyang Peng, Yuxin Sun, Zihang Liu, Fushan Li, Yuke Zhu, Jianbo Zhu, Hao Wu, Nuo Qu, Wenjing Shi, Lei Jiao, Fengkai Guo, Wei Cai, Haijun Wu, and Jiehe Sui, *Semiconductor-Semimetal composite engineering enabling record-high thermoelectric power density for low-temperature energy harvesting*, Adv. Funct. Mater. **34**, 2401763 (2024).

[31] Yifang Huang, Jingdan Lei, Heyang Chen, Zhengyang Zhou, Hongliang Dong, Shiqi Ynag, Haotian Gao,

TIan-Ran Wei, Kunpeng Zhao, and Xun Shi, *Intrinsically high thermoelectric performance in near-room temperature α-MgAgSb materials*, Acta Mater. **249**, 118847 (2023).

[32] Liangjun Xie, Jiawei Yang, Ziyu Liu, Nuo Qu, Xingyan Dong, Jianbo Zhu, Wenjing Shi, Hao Wu, Guyang Peng, Fengkai Guo, Yang Zhang, Wei Cai, Haijun Wu, Hangtian Zhu, Huaizhou Zhao, Zihang Liu, and Jiehe Sui, *Highly efficient thermoelectric cooling performance of ultrafine-grained, and nanoporous materials*, Mater. Today **65**, 5 (2023).

[33] Huaizhou Zhao, Jiehe Sui, ZhongJia Tang, Yucheng Lan, Qing Jie, Daniel Kraemer, Kenneth McEnaney, Arnold Guloy, Gang Chen, and Zhifeng Ren, *High thermoelectric performance of* MgAgSb*-based materials*, Nano Energy **7**, 97 (2014).

[34] Pingjun Ying, Lennart Wilkens, Heiko Reith, Nicolas Perez Rodriguez, Xiaochen Hong, Qiongqiong Lu, Christian Hess, Kornelius Nielsch, and Ran He, *A robust thermoelectric module based on* $MgAgSb/Mg_3(Sb,Bi)_2$ *with a conversion efficiency of 8.5%, and a maximum cooling of 72 K*, Energy Environ. Sci. **15**, 2557 (2022).

[35] Daniel. Kraemer, Jiehe. Sui, Kenneth. McEnaney, Huaizhou Zhao, Qing Jie, Zhifeng Ren, and Gang Chen, *High thermoelectric conversion efficiency of* MgAgSb*-based material with hot-pressed contacts*, Energy Environ. Sci. **8**, 1299 (2015).

[36] Bin Zhu, Xixi Liu, Qi Wang, Yang Qiu, Zhong Shu, Zuteng Guo, Yao Tong, Juan Cui, Meng Gu, and Jiaqing He, *Realizing record high performance in n-type* Bi_2Te_3*-based thermoelectric materials*, Energy Environ. Sci. **13**, 2106 (2020).

[37] Bingchao Qin, Dongyang Wang, Xixi Liu, Yongxin Qin, Jin-Feng Dong, Jiangfan Luo, Jing-Wei Li, Wei Liu, Gangjian Tan, Xinfeng Tang, Jing-Feng Li, Jiaqing He, and Li-Dong Zhao, *Power generation, and thermoelectric cooling enabled by momentum, and energy multiband alignments*, Science **373**, 556 (2021).

[38] Zihang Liu, Naoki Sato, Weihong Gao, Kunio Yubuta, Naoyuki Kawamoto, Masanori Mitome, Keiji Kurashima, Yuka Owada, Kazuo Nagase, Chul-Ho Lee, Jangho Yi, Koichi Tsuchiya, and Takao Mori, *Demonstration of ultrahigh thermoelectric efficiency of* ∼7.3% *in* Mg_3Sb_2/MgAgSb *module for low-temperature energy harvesting*, Joule **5**, 1196 (2021).

[39] Tuo Wang, Hong-Yi Chen, Peng-Fei Qiu, Xun Shi, and Li-Dong Chen, *Thermoelectric properties of* Ag_2S *superionic conductor with intrinsically low lattice thermal conductivity*, Acta Phys. Sin. **68**, 090201 (2019).

[40] Tea-Yon Kim, Yujue Wang, Austin L. Raithel, and Thomas W. Hamann, *Real-time observation of the diffusion progression from liquid to solid state of transition metal complexes*, ACS Energy Lett. **5**, 583 (2020).

[41] Jing Shuai, Hee Seok Kim, Yucheng Lan, Shuo Chen, Yuan Liu, Huaizhou Zhao, Jiehe Sui, and Zhifeng Ren, *Study on thermoelectric performance by* Na *doping in nanostructured* $Mg_{1-x}Na_xAg_{0.97}Sb_{0.99}$, Nano Energy **11**, 640 (2015).

[42] Zihang Liu, Yongsheng Zhang, Jun Mao, Weihong Gao, Yumei Wang, Jing Shuai, Wei Cai, Jiehe Sui, and Zhifeng Ren, *The microscopic origin of low thermal conductivity for enhanced thermoelectric performance of* Yb *doped* MgAgSb, Acta Mater. **128**, 227 (2017).

[43] Amandine Duparchy, Léo Millerand, Julia Camut, Silvana Tumminello, Hasbuna Kamila, Radhika Deshpande, Aidan Cowley, Eckhard Mueller, and Joohannes de Boor, *Establishing synthesis-composition-property relationships for enhanced, and reproducible thermoelectric properties of* MgAgSb, J. Mater. Chem. A **10**, 21716 (2022).

[44] Joseph Callaway, *Model for lattice thermal conductivity at low temperatures*, Phys. Rev. **113**, 1046 (1959).

[45] Pingjun Ying, Ran He, Jun Mao, Qihao Zhang, Heiko Reith, Jiehe Sui, Zhifeng Ren, Kornelius Nielsch, and Gabi Schierning, *Towards tellurium-free thermoelectric modules for power generation from low-grade heat*, Nat. Commun. **12**, 1121 (2021).

[46] Xiaofan Zhang, Nan Chen, Kaiwei Guo, Qintuo Zhang, Qi Zhao, Jingkun Xu, Hangtian Zhu, and Huaizhou Zhao, *High cooling, and power generation performance of α-MgAgSb with intrinsic low lattice thermal conductivity*, Mater. Today Phys. **44**, 101451 (2024).

[47] Xun Shi and Jian He, *Thermopower, and harvesting heat*, Science **371**, 343 (2021).

[48] Yucheng Lan, Austin Jerome Minnich, Gang Chen, and Zhifeng Ren, *Enhancement of thermoelectric figure-of-merit by a bulk nanostructuring approach*, Adv. Funct. Mater. **20**, 357 (2010).

[49] https:/cstr.cn/31113.02.CSNS.GPPD.

[50] Zhijia Han, Zhigang Gui, Y. B. Zhu, Peng Qin, Bo-Ping Zhang, Wenqing Zhang, Li Huang, and Weishu Liu, *The electronic transport channel protection, and tuning in real space to boost the thermoelectric performance of* $Mg_{3+\delta}Sb_{2-y}Bi_y$ *near room temperature*, Research **2020**, 1672051 (2020).

[51] S. S. Li, *Scattering mechanisms and carrier mobilities in semiconductors*, Semi. Phys. Quant. Electron. Optoelectron. 211 (2006).

[52] Chaoliang Hu, Kaiyang Xia, Chenguang Fu, Xinbing Zhao, and Tiejun Zhu, *Carrier grain boundary scattering in thermoelectric materials*, Energy Environ. Sci. **15**, 1406 (2022).

[53] G. Kresse and J. Furthmüller, *Efficiency of ab-initio total energy calculations for metals and semiconductors using a plane-wave basis set*, Comput. Mater. Sci. **6**, 15 (1996).

[54] John P. Perdew, Kieron Burke, and Matthias Ernzerhof, *Generalized gradient approximation made simple*, Phys. Rev. Lett. **77**, 3865 (1996).

[55] Alex D. Becke and Erin R. Johnson, *A simple effective potential for exchange*, J. Chem. Phys. **124**, 221101 (2006).

[56] Fabien Tran and Peter Blaha, *Accurate band gaps of semiconductors, and insulators with a semilocal exchange-correlation potential*, Phys. Rev. Lett. **102**, 226401 (2009).

[57] Andreas Savin, Reinhard Nesper, Steffen Wengert, and Thomas F. Fässler, Angew. Chem., Int. Ed. Engl. **36**, 1808 (1997).

[58] Atsushi Togo, *First-principles phonon calculations with phonopy, and* PHONO3PY, J. Phys. Soc. Jpn. **92**, 012001 (2023).